coatings

MDPI

Article

Damage Characteristics of Aluminum-Coated Grating Irradiated by Nanosecond Pulsed Laser

Jiamin Wang [1,2], Kuo Zhang [1], Yanhui Ji [1,2], Jinghua Yu [1,2], Jirigalantu [3], Wei Zhang [3], Wenhao Li [3], Changbin Zheng [1,*] and Fei Chen [1,*]

[1] State Key Laboratory of Laser Interaction with Matter, Changchun Institute of Optics, Fine Mechanics and Physics, Chinese Academy of Sciences, 3888 Dongnanhu Road, Changchun 130033, China; wangjiamin18@mails.ucas.ac.cn (J.W.); zhangkuo_fx@163.com (K.Z.); jiyanhui18@mails.ucas.ac.cn (Y.J.); yjh10111510@163.com (J.Y.)

[2] University of Chinese Academy of Sciences, Beijing 100049, China

[3] National Engineering Research Center for Diffraction Gratings Manufacturing and Application, 3888 Dongnanhu Road, Changchun 130033, China; jiri5998@163.com (J.); zhangwei1990@ciomp.ac.cn (W.Z.); liwh@ciomp.ac.cn (W.L.)

* Correspondence: zhengchangbin@ciomp.ac.cn (C.Z.); feichenny@126.com (F.C.)

Abstract: An aluminum-coated grating (ACG) is a core component of laser systems and spectrometers. Understanding damage to the ACG induced by nanosecond lasers is critical for future high-power laser applications. In this study, we applied finite element simulation and practical experimentation to investigate the characteristics of ACG damage. Based on a coupling model using fluid heat transfer with the level-set method, we simulated the damage caused to an ACG by a 1064 nm nanosecond single pulse laser. The theoretical modeling showed that the ridge and bottom corners of the grid will be preferentially damaged, and the simulated damage threshold will range from 0.63 J/cm^2 to 0.95 J/cm^2. We performed a one-on-one damage test according to the ISO21254 standard to investigate the failure condition of 1800 l/mm ACGs; the laser-induced damage threshold (LIDT) was 0.63 J/cm^2 (1064 nm, 6.5 ns). Microscopy images showed that the damaged area decreased with decreasing laser fluence, and scanning electron microscopy measurements showed that the main damage mechanism was thermodynamic damage, and that damage to the grid occurred first. The results of the experiments and simulations were in good agreement.

Keywords: nanosecond pulsed laser; aluminum-coated gratings; damage mechanism; LIDT; morphology

Citation: Wang, J.; Zhang, K.; Ji, Y.; Yu, J.; Jirigalantu; Zhang, W.; Li, W.; Zheng, C.; Chen, F. Damage Characteristics of Aluminum-Coated Grating Irradiated by Nanosecond Pulsed Laser. *Coatings* **2022**, *12*, 701. https://doi.org/10.3390/coatings12050701

Academic Editor: Alessio Lamperti

Received: 6 April 2022
Accepted: 19 May 2022
Published: 20 May 2022

1. Introduction

In recent years, numerous research efforts have been made to understand the damage mechanisms and the ablation process in the interaction between lasers and gratings [1–3]. Gratings are an important pulse compression element in high-peak power laser systems [4,5], and their laser-induced damage threshold (LIDT) both limits the laser energy and affects the operating cost of optics renewal or replacement. Gratings, whose general structure comprises a metal film deposited on a glass substrate, with regular grooves on the surface of the metal film, also play a key role in spectroscopy devices. In laser systems and photoelectric imaging equipment, the LIDT of gratings is a very important indicator [6]. Measuring the LIDT of gratings and studying their laser damage characteristics and mechanisms is of great importance for the optimization of gratings and the application of high-power lasers.

Damage to thin-film materials by nanosecond pulsed lasers involves complex physical mechanisms, such as impurity-induced phase explosion [7,8], phase transition-induced mass removal [9], plasma-induced plasma expansion [10], plasma shielding [11], and shock wave effects [12–14]. To date, with the improvement of laser technology, researchers

have studied the damage mechanisms and damage thresholds of various lasers acting on different gratings [15–17], including those of continuous lasers on multilayer dielectric film gratings [18–20], and those of nanosecond pulsed lasers and ultrafast lasers acting on gold, multilayer dielectric, and hybrid multilayer dielectric film gratings [21]. However, aluminum-coated gratings are also widely used in spectrometers, aperture cameras, and detection devices because of their low cost, high practicability, stable reliability, and high diffraction efficiency, but there are few reports on the damage caused to aluminum-coated gratings irradiated by 1064 nm nanosecond pulsed lasers.

Moreover, previous research has generally focused on the influence of the laser parameters on grating damage, such as wavelength [22], pulse width [15], spot [23] and pulse accumulation [24] effects; the differences in laser damage caused by different grating structure characteristics [25] such as the substrate material, the thickness of the film, the stacking of the films, and the manufacturing process; and the damage induced by impurities, defects [26], and contamination [27]. Most of the research methods have been based on experiments, with a lack of reports on the use of simulation models to predict the LIDT of metal gratings irradiated by nanosecond lasers. The dynamic evolution process of damage to gratings by lasers also needs to be further studied. Thus, the damage mechanism of nanosecond pulsed laser irradiation on ACGs needs to be further clarified, and the process underlying laser-induced damage on the grating structure needs to be further investigated.

To understand the properties of ACGs under nanosecond pulsed laser irradiation, we built a simulation model coupling fluid heat transfer and the level-set method, and we also performed an experimental study using nanosecond pulsed laser irradiation (1064 nm, 6.5 ns). We tested the LIDT and damage morphology of ACGs with nanosecond lasers at different energy densities. In addition, some typical morphologies were further analyzed. The simulation results were compared with the experimental results to verify the accuracy of the model. Our work has implications for grating design and the prediction of grating LIDT.

2. Materials and Methods

2.1. Sample Customization

The ACGs were designed with a groove density of 1800 l/mm and manufactured by the National Engineering Research Center for Diffraction Gratings Manufacturing and Application of China. A schematic diagram of the grating is shown in Figure 1. Resin adhesive with a thickness of 30 μm was spun onto a 40 mm × 40 mm × 6 mm K9 glass substrate. An aluminum film approximately 125 nm thick, with a purity of 99.9999%, was used to fabricate a surface-relief grating structure by E-beam evaporation. The grating groove depth was 105 nm and the thickness of the remaining layer was 20 nm. Photoresist material was spun onto the aluminum film, and a photoresist grating structure was manufactured using a holographic method. The structures of the photoresist gratings were transferred to the aluminum film layer by reactive ion-beam etching. Finally, gratings with a diffraction efficiency of 70% were fabricated.

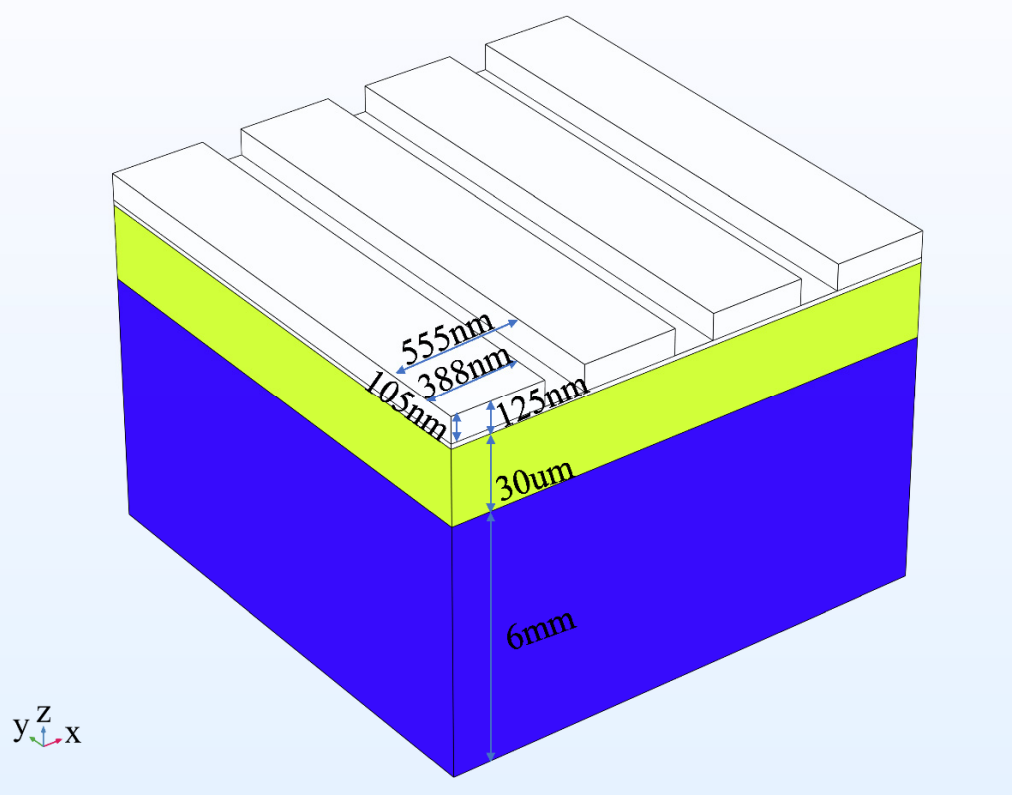

Figure 1. Schematic diagram of the grating structure.

2.2. Simulation Model

To better understand the characteristics of nanosecond pulse laser damage to ACGs, the process of nanosecond pulse laser irradiation of ACGs was simulated. When ACGs are irradiated by a nanosecond laser, complex damage mechanisms need to be considered, including mass removal, interfacial tracking, and temperature-induced changes to the thermal physical properties of the material. In addition, the gravity of the material itself, the recoil pressure gas expansion, and Darcy resistance all have an important influence on ablation morphology. Compared with the moving mesh method (ALE) and the volume of fluid (VOF) method, the level-set method can simulate the topological structure changes more accurately. Under an evolution process, the mesh automatically adjusts the density to track the discontinuous motion locally, and only a small amount of computation is required to improve the calculation accuracy and discontinuous resolution. Therefore, based on a finite element method (FEM), the level-set method was coupled with fluid heat transfer to numerically simulate the process of damage to ACGs by nanosecond pulse laser irradiation, and to reveal the damage features and mechanism.

2.2.1. Theoretical Method

To simplify the calculation, we made following assumptions before building the model: (i) the molten liquid and the surrounding air exhibit incompressible laminar flows, (ii) the evaporated vapor is an ideal gas and does not absorb the incident laser, and (iii) the Knudsen layer can be ignored.

When the nanosecond pulse laser interacts with ACGs, the computational domains can be expressed by the conservation of energy, momentum, and the level-set method. The calculation formulas are shown in Equations (1)–(3):

$$\rho C_p \frac{\partial T}{\partial t} + \rho C_p \vec{u} \cdot \nabla T = \nabla \cdot (k \nabla T) + \delta[\alpha S - L_V v_e \rho_l + \xi k_B (T_0^4 - T^4)] \quad (1)$$

$$\rho\frac{\partial\vec{u}}{\partial t}+\rho(\vec{u}\cdot\nabla)\vec{u}=\nabla\cdot[-pI+\mu(\nabla\vec{u}+(\nabla\vec{u})^{T})]+\rho\vec{g}+\delta(\sigma\kappa\nabla\phi\vec{i}-p_{recoil}\vec{i}+\frac{\partial\sigma}{\partial T}\frac{\partial T}{\partial x}\vec{j}) \quad (2)$$

$$\frac{\partial\phi}{\partial t}+\vec{u}\cdot\nabla\phi-\delta m_0(\frac{V_{f,v}}{\rho_v}+\frac{V_{f,l}}{\rho_l})+\gamma\nabla\cdot(\phi(1-\phi)\frac{\nabla\phi}{|\nabla\phi|}-\varepsilon\nabla\phi)=0 \quad (3)$$

Equation (3) represents the conservation of energy, where ρ, C_p, u, and k are the density, specific heat, velocity, and coefficient of thermal conductivity, respectively. Their properties depend on the temperature. δ is the delta function, defined as:

$$\delta=6|\phi(1-\phi)||\nabla\phi| \quad (4)$$

$$S=(1-R)\cdot\frac{E}{\pi r_0^2 t_p}\exp(-x^2/r_0^2)\cdot\exp(-\alpha(y_0-y))\cdot\alpha\cdot\exp(-2.77\cdot\frac{(t-t_0)^2}{t_p^2}) \quad (5)$$

The second term on the right-hand side of the equals sign represents the heat source. This includes the absorption of the laser heat shown as δS, the latent heat dissipated by evaporation, $\delta L_v v_e \rho_l$, and the spontaneous radiation of heat from the surface of the material, $\delta\xi k_B\ ({T_0}^4-T^4)$. Since we calculated the microstructure of the grating and only calculated two grids, we ignored the influence of thermal convection, and we applied periodic boundary conditions on the two sides of the geometric model.

At the vapor–liquid interface, we considered the hydrodynamic boundary, as shown in Equation (2). It takes into account the normal gravity, ρg; the surface tension, $\delta\sigma\kappa\nabla\phi i$; the recoil pressure, $\delta p_{recoil} i$; and the driving force, $\delta\partial\sigma/\partial T\cdot\partial T/\partial x\, j$ caused by the gradient of the surface tension. Based on the level-set method to describe the solid–liquid and gas–liquid interfacial motion, as shown in Equation (3), it considers the effect of evaporation on the interfacial motion, where $V_{f,v}$ and $V_{f,l}$ are the gas and liquid volume fractions, respectively; it employs γ to calculate the initialized interface velocity, and ε is the reciprocal distance of the horizontal set interface.

2.2.2. Parameter Settings

In this subsection, we show some of the important formulas and key parameters. The saturation vapor pressure of metal vapor P_{sat} was determined by the Clausius–Clapeyron equation, and this is shown in Equations (6) and (7):

$$P_{sat}(T)=P_{amb}\exp(\frac{L_v M_{Al}}{k_B T}(\frac{T}{T_v}-1)) \quad (6)$$

$$P_{recoil}(T)=0.54P_{sat}(T) \quad (7)$$

where P_{amb} is the atmospheric pressure, M_{Al} is the molar mass of aluminum, and P_{recoil} is the recoil pressure of the evaporating vapor.

Some important parameters of the simulation are listed in Table 1.

Table 1. Key parameter list of the simulation.

Parameter	Symbol	Expression or Value
Pulse of width	τ_p, ns	6.5
Radius of spot	R_0, μm	300
Single pulse energy	E, mJ	1.78–5.85
Boiling point	Tb, K	2793
Melting point	Tm, K	933
Gas phase density	ρ_v, kg/m^3	30
Liquid phase density	ρ_l, kg/m^3	2385
Solid phase density	ρ_s, kg/m^3	2700
Thermal conductivity of the solid phase	k_s, W/(m·K)	238

Table 1. *Cont.*

Parameter	Symbol	Expression or Value
Thermal conductivity of the liquid phase	k_l, W/(m·K)	100
Specific heat of the solid phase	Cp_s, J/(kg·K)	917
Specific heat of the liquid phase	Cp_l, J/(kg·K)	1080
Dynamic viscosity of the liquid phase	μ_l, kg/(m·s)	0.05
Dynamic viscosity of the solid phase	μ_s, kg/(m·s)	$\mu_l \times 10^5$
Latent heat of fusion	L_f, J/kg	3.896×10^5
Latent heat of evaporation	L_v, J/kg	9.462×10^6
Radiation emissivity	ξ	0.2
Surface tension coefficient	σ, N/m	$0.95 \times (1 + 0.03 \times (1 - T/T_m))^{1.67}$
Absorptivity	α	$354.67 \times ((-1 + 1.25 \times 10^{-2} \cdot T) \times 10^{-8})^{1/2}$
Dynamic viscosity of the gas phase	μ	0
Gas evaporation coefficient	β	0.82

2.3. Experimental Method

To further reveal the characteristics of the damage to ACGs, and to verify the effectiveness of the simulation model, we carried out experimental research. Figure 2 shows a schematic diagram of the experimental setup for the laser damage test. The laser damage experiments were performed with a Nd:YAG laser (1064 nm, 6.5 ns) at an incidence angle of 0° with TE polarization, which produced a near-Gaussian spatial profile. The energy stability (RMS) was less than or equal to 1%. The emitted laser energy was adjusted using an attenuator consisting of a half-wave plate and a polarizer. The reflected beam passed through a beam splitter to a calibrated energy meter (Ophir, PE50-DIF-C, calibration uncertainty ± 3%), which was used for real-time monitoring of energy, and onto the target vertically, with the transmitted beam focused on the center of the target surface through a plane convex lens (f = 100 mm). The radius of the focused beam was 300 μm, based on a knife-edge test method where the step size of the knife-edge method was 1 μm. The ACGs were placed on a two-dimensional displacement platform (1 μm accuracy), and the position of the laser action was precisely controlled by a computer. Dust was removed from the surface of the sample before the experiment began. The experiment was performed in air under class 10,000 laboratory conditions. Based on the one-on-one damage threshold test method, the damage threshold was tested at 100 points with each laser fluence. The laser fluence was gradually increased and the damage morphology was observed using a Nomarski microscope (EB-4, Taiwan Yiye International Co., Ltd., Taiwan, China), and using SEM (S-4800, HITACHI, Tokyo, Japan). For determining the LIDT, damage was defined as a visible change in surface morphology under an off-line microscope, according to ISO21254 [28].

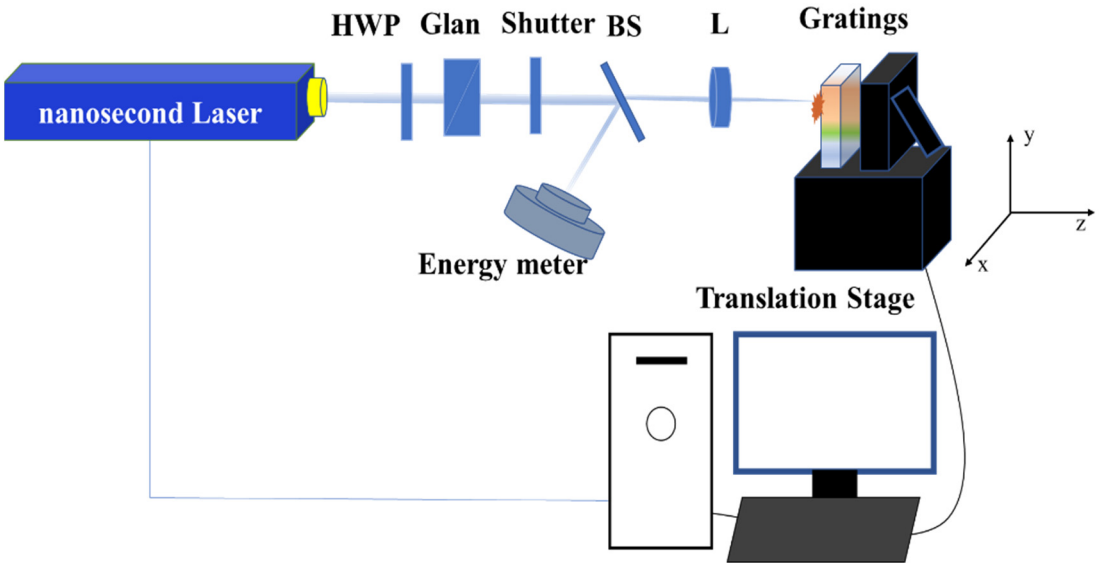

Figure 2. Diagram of the experimental setup of nanosecond laser damage to the ACGs.

3. Results and Discussion

3.1. Damage Morphologies

3.1.1. Damage Morphology by Different Laser Fluences

The ACG damage morphology at different laser fluences is shown in Figure 3. The diameter of the maximum ablation area was 1208.2 μm at 333.87 J/cm^2, and the size of the minimum ablation was 373.5 μm at 0.72 J/cm^2. When the laser fluence was decreased to 0.63 J/cm^2, no visible damage occurred. The pattern of variation in the damaged area of the aluminum grating against laser fluence was similar to the results of Zheng et al. [29], who studied picosecond laser action on aluminum alloys. As shown in Figure 4, the ablation feature size increased with increasing laser fluence, and when the laser fluence reached a certain level, the growth rate of the ablation area size decreased and gradually tended to saturation.

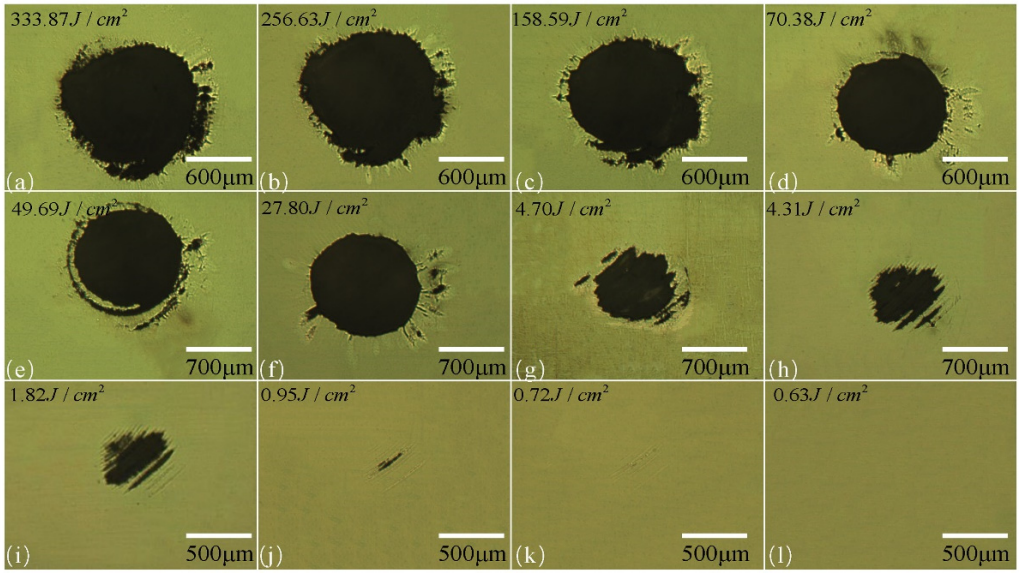

Figure 3. The damage morphology under different laser fluence.

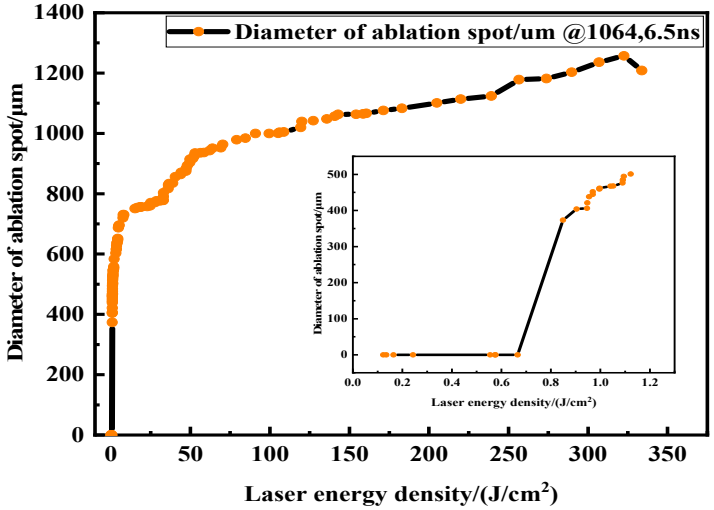

Figure 4. Curve of the damage area vs. laser fluence.

When irradiated at a higher laser fluence, the surface-relief grating structure and epoxy resin layer were ablated, forming black substances bound to the K9 glass substrate and black ablation pits, with pale yellow areas around the black ablation profile. During laser irradiation, the aluminum film absorbed the laser energy, then reached its melting point and the molten material was ejected from around the ablation pit. In contrast to the morphology of ultrafast laser damage to a grating, the ablation pit formed with the nanosecond pulse laser was irregular, and there were molten splashes attached around the ablation pit. This indicated that when ACGs were irradiated with a 6.5 ns single pulse laser, the aluminum film that absorbed the laser energy had enough time to release heat to the environment, and therefore at high flux the damage area may be larger than the laser irradiation area. Around the large ablation pits, there were small ablation pits, which were probably due to the presence of isolated surface defects (damage precursors) [30]. There will be grease and dust [27] from the grating manufacturing process, bubbles from the coating process, and residual debris from the grating etching process present. In the process of laser irradiation, because the absorption coefficient of the impurities is greater than that of the film itself, it will absorb more laser energy and be easier to damage. Moreover, the existence of impurities leads to uneven heating, temperature gradients, and thermal expansion. When the stress exceeds the adhesion strength of the film, peeling damage will occur, resulting in damaged areas that are generally larger than the spot diameter.

3.1.2. Typical Damage Morphologies

Figure 5 shows the typical morphology of ACGs induced by thermal damage. Figure 5a shows the complete damage morphology, comprising four types of areas: from the center to the edge, the central ablation area, the melt sputtering area, the grid melting area, and the grid incomplete damage area; corresponding to areas I, II, III and IV of Figure 5 respectively. Figure 5b displays the four types of topography in local magnification at 2000 times, and Figure 5c,d show the damage morphology of the grids at 5000 times and 20,000 times magnification, respectively. In the central area, the ACGs were completely ablated and formed ablation pits. This destroyed the aluminum film in the central area and, due to the resulting poor conductivity, it became bright under the scanning electron microscope. The molten ablations were sprayed around the pits. The main ACG damage mechanism from nanosecond pulsed laser irradiation was thermal damage. Around the damage profile, where the irradiated laser energy was minimal, the grids were slightly damaged.

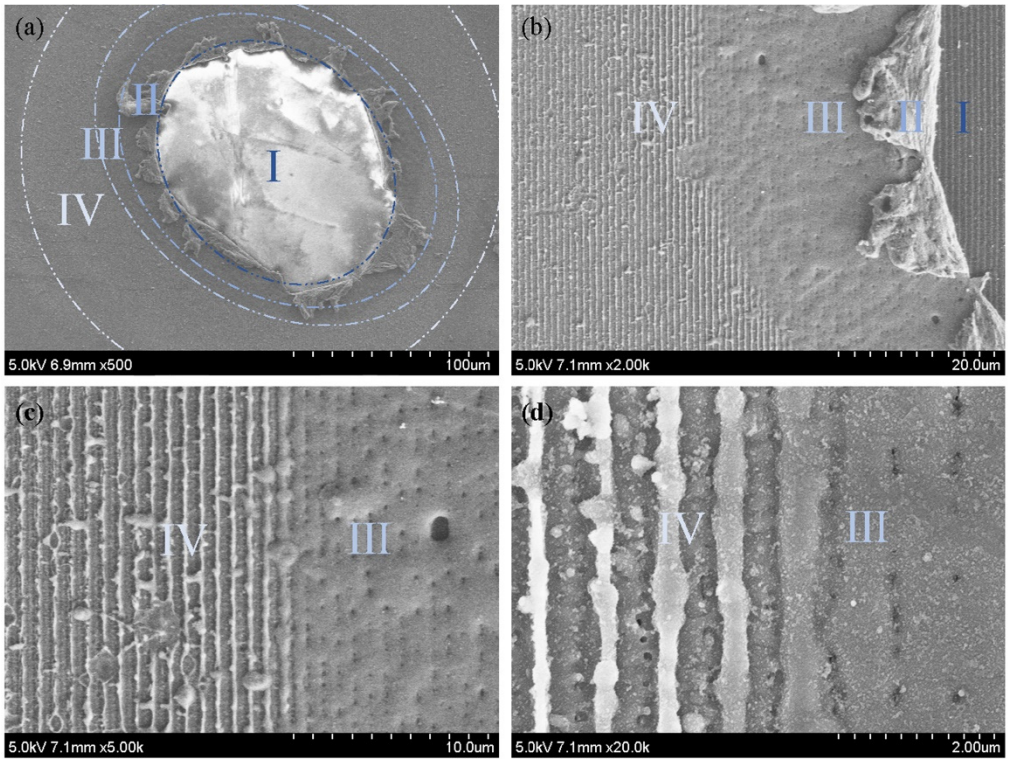

Figure 5. Thermal ablation melting damage morphology of aluminum grating at 325 J/cm^2 (**a**) 500×; (**b**) 2000×; (**c**) 5000×; (**d**) 20,000×.

Figure 6 shows the ACG damage morphology from a 0.72 J/cm^2 laser fluence: the total damage is shown in Figure 6a, and Figure 6b–d show the magnified views of the blue frame, red frame, and yellow frame, respectively. It can be seen that there was a big difference in the damage morphology between Figures 5 and 6. The possible reason is that at low laser fluence, the grating modulated the laser light field distribution, which made the surface damage morphology of the ACGs appear as stripes. According to Figure 6a, the damage mechanism behind this was thermodynamic damage caused by impurities. When the laser irradiated the ACGs, the impurities at the interface of the film preferentially absorbed the laser energy and generated thermal expansion. When the thermal stress generated by the thermal expansion reached the fracture strength of the film, the film peeled off. As shown in Figure 6b, bulges were formed in the low laser fluence distribution region, and the film fell off in the high laser fluence region. Figure 6c shows that as the laser fluence decreased, the grids were slightly damaged. Only on the right side of Figure 6c can we see the pristine grid line, which shows that the damage to the grids was caused by thermal effects before any melting damage to the ACGs; which had a negative effect on the function of the ACG. Next, we simulated grid damage of the ACGs at the lower laser fluence.

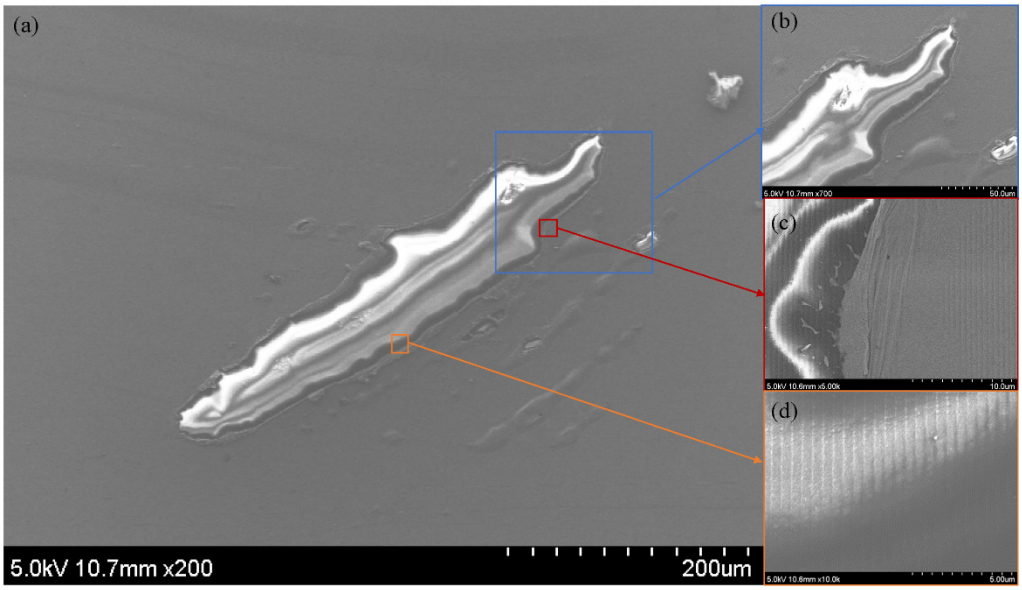

Figure 6. Thermodynamic damage morphology of ACGs at 0.72 J/cm^2.

3.1.3. Damage Morphology of Preferential Damage of Grid Ridge

In addition to the above-mentioned damage morphology characteristics, we found that most of the damage morphologies displayed the phenomenon of grid ridge priority damage when the laser was at a vertical incidence. Taking the damage morphology at 0.95 J/cm^2 as an example, as shown in Figure 7, it was found that it was easy to cause ablation and film peeling at the grid ridge. The analysis suggested that when the laser irradiated the ACGs vertically, it was modulated by the grating, and the laser light field was redistributed, so there was an enhancement effect on the electric field at the grating ridge, and more energy was deposited at the grating ridge, which made damage more likely to occur.

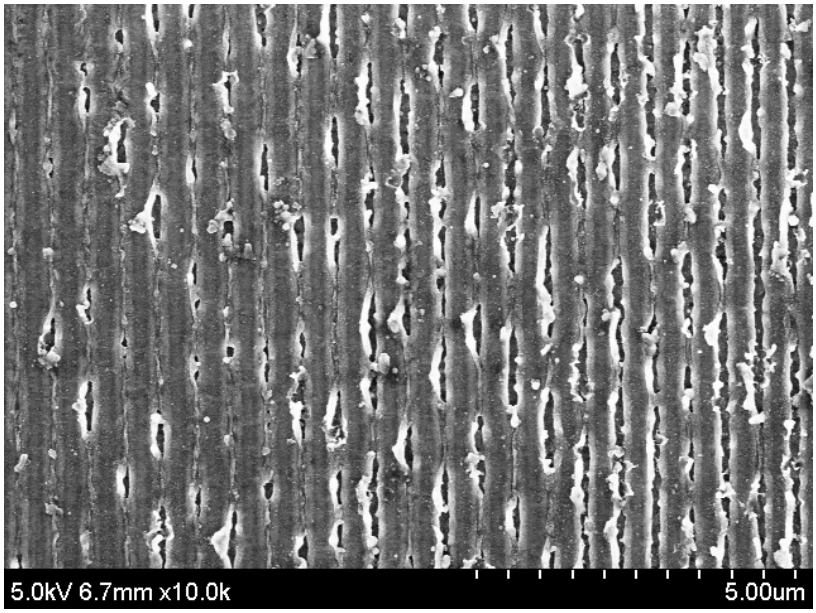

Figure 7. Damage morphology showing preferential damage of grid ridge at 0.95 J/cm^2.

We simulated the damage morphology of the grating at 0.95 J/cm^2, and to save computational resources, we only simulated the grating ridge to illustrate the preferential ridge ablation phenomenon. According to the parameters set in Table 1, the spot radius

was 300 µm. We obtained the temperature field distribution and damage evolution of the grating at 0.95 J/cm^2. The distribution is shown in Figure 8. It indicates that the melting point of the material will be first reached at the ridge of the grating; the top corner of the gate ridge is susceptible to damage. Moreover, in the remaining layer region, due to the direct irradiation of the grating and the thermal conduction of the gate ridge, the temperature maximum will occur in the middle region of the grid pitch, and so the bottom corner of the gate ridge will also be prone to damage. Figure 8a and b clearly illustrate the higher temperatures in the top corners, bottom corners, and pitch regions of the ridges.

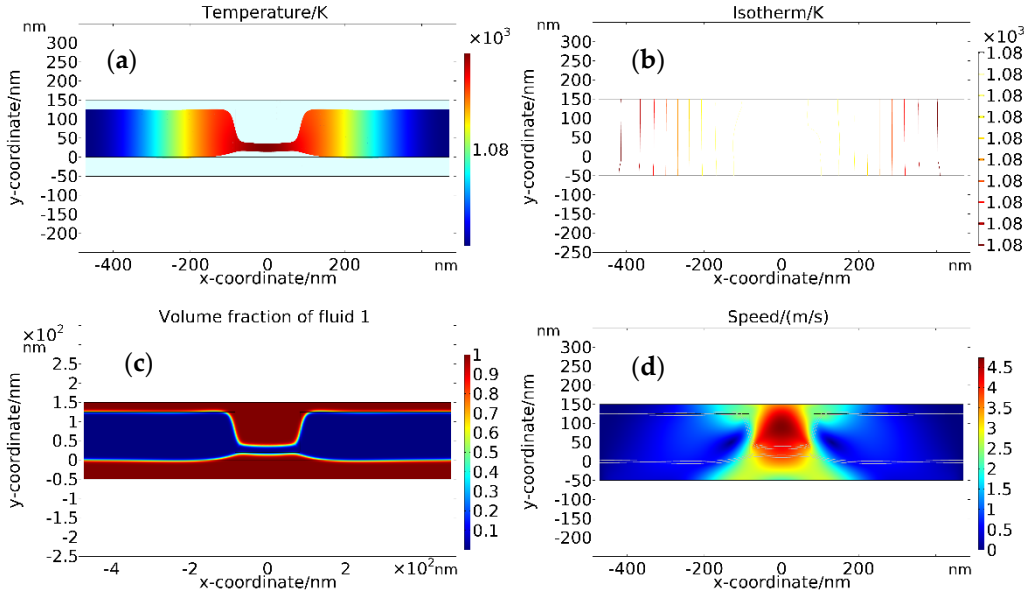

Figure 8. The damaged ridges of ACGs with single-pulsed nanosecond laser irradiation at 0.95 J/cm^2: (**a**) Temperature field distribution, (**b**) Isotherm map, (**c**) Volume fraction, (**d**) Velocity field.

Figure 8c is a solid–liquid volume fraction cloud diagram, which shows the ablative deformation of the ridge. The red region represents the liquid and gaseous states, and the blue region represents the solid state. Due to the laser action, the solid region gradually becomes irregular and deviates from the original regular grating structure. The top and bottom corners of the ridge will change from the original right angles to round corners, and finally melt. Figure 8d is the cloud diagram of the ablation rate during the laser action period. It can be seen that the ablation rate at the top and bottom corners of the ridge is faster than in other areas.

3.2. Comparison of LIDT

The LIDTs were compared and analyzed, and the comparison results are shown in Figure 9. The criterion for damage was that the corresponding laser fluence was at the LIDT when the maximum temperature of the grating exceeded its melting point (933 K).

Figure 9a shows the time evolution process for the maximum temperature of the material at different laser energy densities. Since the grating temperature hardly changed under the continuous heating of the 2 ns single pulse laser, we only show the temperature evolution process of the grating over 3 ns. From this, it can be seen that melting damage occurred when the laser energy density was 0.95 J/cm^2. The temperature did not exceed the melting point when the laser energy density was 0.67 J/cm^2, so the LIDT of the ACGs was determined by simulation over a range from 0.67 J/cm^2 to 0.95 J/cm^2. To verify the results of the simulation, we performed an LIDT test on the ACGs based on Section 2.3. The nanosecond pulsed laser damage probability curve for ACGs under different laser fluences is shown in Figure 9b. It can be seen that the probability of damage to the grating at 0.63 J/cm^2 was 0, and at 0.67 J/cm^2 it was 100%, We took the maximum laser fluence

with zero probability of damage as the criterion for evaluating the LIDT. Therefore, the laser damage threshold of ACGs was determined to be 0.63 J/cm^2. The LIDT found in the experiment was 0.67 J/cm^2. In general, the LIDT calculated by the simulation agreed well with the experimental one. The reason for the difference between the simulation and the experiment could be that the simulation did not take into account the influence of impurities, which made the simulation LIDT larger than that found in the experiment.

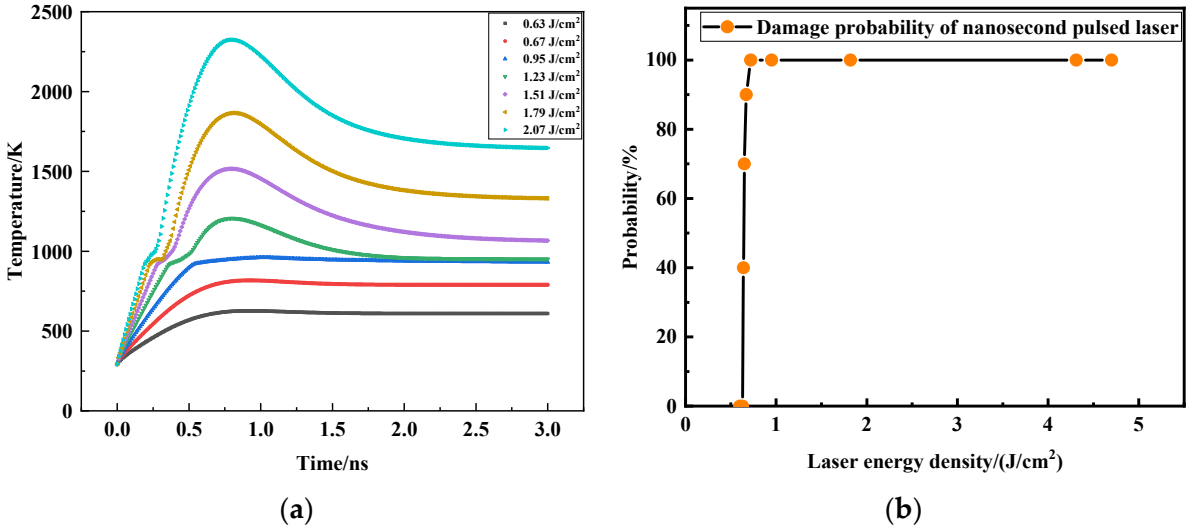

Figure 9. Comparison of LIDT between experimental and simulated data: (**a**) Evolution of temperature with time for different laser energy densities, (**b**) The damage probability curve for ACGs under different laser fluence.

4. Conclusions

In this study, we explored the characteristics of ACG damage from a nanosecond single pulse laser, through the combination of simulation and experimentation. Based on an FEM, the temperature and ablation velocity fields of the ACGs were simulated using a method coupling fluid heat transfer and the level-set method. It was found that the top and bottom corners of the ridge will be hotter and accordingly, material removal will occur here first. Using a parametric scanning method, the LIDT of the ACGs damaged by nanosecond pulsed laser was projected to be 0.67–0.95 J/cm^2, and we found that the top and bottom corners of the ridge will be hotter and accordingly, material removal will occur here first. Further to this, we performed an experimental study based on a one-on-one damage threshold test method to investigate the characteristics of ACG damage by a pulsed nanosecond laser. The LIDT of the ACGs was 0.63 J/cm^2 (1064 nm, 6.5 ns) and the damage morphology suggested that the main physical mechanisms were thermodynamic damage caused by the film falling off, and ablation. We found that the pillars of the ACGs were damaged first during the process of nanosecond single pulse irradiation, which was similar to the simulation results. Overall, the experiment LIDT results were in accordance with the simulation results. Comparing the results, the LIDT determined in the simulation was slightly larger than that found in the experiment since the defects in the material were not considered in the simulation. The results here shown are of great significance for the design of grating ridges and laser applications. This method could be extended to three dimensions in the future, to take into account more influencing factors for multi-physics coupling, such as shock wave transmission within the grating, phase explosion, and plasma shielding at high laser energy density.

Author Contributions: Conceptualization, J.W. and C.Z.; methodology, F.C.; software, K.Z. and W.Z.; validation, J., W.L., F.C. and C.Z.; formal analysis, J.W.; investigation, Y.J. and J.Y.; writing—original draft preparation, J.W.; writing—review and editing, C.Z.; project administration, F.C.;

funding acquisition, F.C., C.Z. and K.Z. All authors have read and agreed to the published version of the manuscript.

Funding: Major Innovation Project of CIOMP, CAS (E10302Y3M0), Fund Project of the State Key Laboratory of Laser-Matter Interaction (SKLLIM2105), National Natural Science Foundation (61904178), Member of the Youth Innovation Promotion Association of the Chinese Academy of Sciences (2020227), Funding of 'Xuguang Talents' from CIOMP, National Natural Science Foundation of China (General Program 62075216).

Institutional Review Board Statement: Not applicable.

Informed Consent Statement: Not applicable.

Data Availability Statement: The data presented in this study are available on request from the corresponding author. The data are not publicly available due to confidentiality.

Conflicts of Interest: The authors declare no conflict of interest.

References

1. Zhou, C. Chirped pulse amplification: Review and prospective from diffractive optics. *Chin. Opt. Lett.* **2020**, *18*, 110502. [CrossRef]
2. Strickland, D. Nobel Lecture: Generating high-intensity ultrashort optical pulses. *Rev. Mod. Phys.* **2019**, *91*, 030502. [CrossRef]
3. Amen, N.V. Extreme light infrastructure–nuclear physics (ELI-NP) European Research Centre. *EPJ Web Conf.* **2014**, *66*, 11043.
4. Lozhkarev, V.V.; Freidman, G.I.; Ginzburg, V.N.; Katin, E.V.; Khazanov, E.A.; Kirsanov, A.V.; Luchinin, G.A.; Mal'shakov, A.N.; Martyanov, M.A.; Palashov, O.V.; et al. 200 TW 45 fs laser based on optical parametric chirped pulse amplification. *Opt. Express* **2006**, *14*, 446–454. [CrossRef] [PubMed]
5. Zhang, W.; Fu, S.; Kong, W.; Wang, G.; Xing, F.; Zhang, F.; Zhang, H. Review of pulse compression gratings for chirped pulse amplification system. *Opt. Eng.* **2021**, *60*, 020902. [CrossRef]
6. Glebov, L.B.; Smirnov, V.I.; Stickley, C.M.; Ciapurin, I.V. New approached to robust optics for HEL systems. In *Laser Weapons Technology III*; International Society for Optics and Photonics: Orlando, FL, USA, 2002; Volume 4724.
7. Mazzi, A.; Miotello, A. Simulation of phase explosion in the nanosecond laser ablation of aluminum. *J. Colloid Interface Sci.* **2017**, *489*, 126–130. [CrossRef] [PubMed]
8. Gragossian, A.; Tavassoli, S.H.; Shokri, B. Laser ablation of aluminum from normal evaporation to phase explosion. *J. Appl. Phys.* **2009**, *105*, 103304. [CrossRef]
9. Wang, Y.; Shen, N.; Befekadu, G.; Pasiliao, C.L. Modeling pulsed laser ablation of aluminum with finite element analysis considering material moving front. *Int. J. Heat Mass. Transf.* **2017**, *113*, 1246–1253. [CrossRef]
10. Wang, Y.; Hahn, D.W. A simple finite element model to study the effect of plasma plume expansion on the nanosecond pulsed laser ablation of aluminum. *Appl. Phys. A Mater. Sci. Processing* **2019**, *125*, 1–15. [CrossRef]
11. Nammi, S.; Vasa, N.J.; Gurusamy, B.; Mathur, A.C. Single laser based pump-probe technique to study plasma shielding during nanosecond laser ablation of copper thin films. *J. Phys. D Appl. Phys.* **2017**, *50*, 355204. [CrossRef]
12. Inogamov, N.; Khokhlov, V.; Petrov, Y.; Anisimov, S.; Zhakhovsky, V.V.; Demaske, B.J.; Oleynik, I.I.; Ashitkov, S.I.; Khishchenko, K.V.; Agranat, M.; et al. Ultrashort elastic and plastic shockwaves in aluminum. *AIP Conf. Proc.* **2012**, *1426*, 909.
13. Huang, L.; Yang, Y.; Wang, Y.; Zheng, Z.; Su, W. Measurement of transit time for femtosecond-laser-driven shock wave through aluminum films by ultrafast microscopy. *J. Phys. D Appl. Phys.* **2009**, *42*, 045502. [CrossRef]
14. Ho, J.R.; Grigoropoulos, C.P.; Humphrey, J.A.C. Computational study of heat transfer and gas dynamics in the pulsed laser evaporation of metals. *J. Appl. Phys.* **1995**, *78*, 4696–4709. [CrossRef]
15. Wang, Y.; Cheng, X.; Shao, J.; Zheng, C.; Chen, A.; Zhang, L. The Damage Threshold of Multilayer Film Induced by Femtosecond and Picosecond Laser Pulses. *Coatings* **2022**, *12*, 251. [CrossRef]
16. Zhang, L.; Jia, X.; Wang, Y.; Zhang, Y.; Chen, A.; Shao, J.; Zheng, C. Effect of Femtosecond Laser Polarization on the Damage Threshold of Ta_2O_5/SiO_2 Film. *Appl. Sci.* **2022**, *12*, 1494. [CrossRef]
17. Rasedujjaman, M.; Gallais, L. Polarization dependent laser damage growth of optical coatings at sub-picosecond regime. *Opt. Express* **2018**, *26*, 24444–24460. [CrossRef]
18. Wang, H.; Song, Y.; Yang, Y.; Xian, Y.; You, Y.; Liu, M.; Yuan, Z.; Wei, T.; He, B.; Zhou, J. Simulation and experimental study of laser-induced thermal deformation of spectral beam combination grating. *Opt. Express* **2020**, *28*, 33334–33345. [CrossRef]
19. Kim, I.; So, S.; Mun, J.; Lee, K.H.; Lee, J.H.; Lee, T.; Rho, J. Optical characterizations and thermal analyses of HfO_2/SiO_2 multilayered diffraction gratings for high-power continuous wave laser. *J. Phys. Photon.* **2020**, *2*, 025004. [CrossRef]
20. Xu, J.; Chen, J.; Chen, P.; Wang, Y.; Zhang, Y.; Kong, F.; Cao, H.; Jin, Y.; Shao, J. Continuous-wave laser damage mechanism of a spectral combining grating. *Appl. Opt.* **2019**, *58*, 2551–2555. [CrossRef]
21. Li, Z.; Xia, Z. The damage mechanism and process of metal multi-layer dielectric gratings induced by ps-pulsed laser. *Appl. Surf. Sci.* **2019**, *494*, 977–982. [CrossRef]
22. Kumar, S.; Shankar, A.; Kishore, N.; Mukherjee, C. Laser Induced Damage Threshold of Ta_2O_5 and Ta_2O_5/SiO_2 Films at 532 and 1064 nm. *Optik* **2019**, *176*, 438–447. [CrossRef]

23. Stehlík, M.; Wagner, F.; Zideluns, J.; Lemarchand, F.; Lumeau, J.; Gallais, L. Beam-size effects on the measurement of sub-picosecond intrinsic laser induced damage threshold of dielectric oxide coatings. *Appl. Opt.* **2021**, *60*, 8569–8578. [CrossRef] [PubMed]
24. Han, Y.; Jin, Y.; Kong, F.; Wang, Y.; Zhang, Y.; Cao, H.; Cui, Y.; Shao, J. High-repetition-rate and multi-pulse ultrashort laser damage of gold-coated photoresist grating. *Appl. Surf. Sci.* **2022**, *576*, 151819. [CrossRef]
25. Xie, L.; Zhang, J.; Zhang, Z.; Ma, B.; Li, T.; Wang, Z.; Cheng, X. Rectangular multilayer dielectric gratings with broadband high diffraction efficiency and enhanced laser damage resistance. *Opt. Express* **2021**, *29*, 2669–2678. [CrossRef] [PubMed]
26. Ma, B.; Han, J.; Li, J.; Wang, K.; Guan, S.; Niu, X.; Li, H.; Zhang, J.; Jiao, H.; Cheng, X.; et al. Damage characteristics of dual-band high reflectors affected by nodule defects in the femtosecond regime. *Chin. Opt. Lett.* **2021**, *19*, 081403. [CrossRef]
27. Kafka KR, P.; Hoffman, B.N.; Huang, H.; Demos, S.G. Mechanisms of picosecond laser-induced damage from interaction with model contamination particles on a high reflector. *Opt. Eng.* **2020**, *60*, 031009. [CrossRef]
28. *ISO 21254-2: 2011*; Lasers and Laser-Related Equipment—Test Methods for Laser-Induced Damage Threshold—Part 2: Threshold Determination. International Organization for Standardization (ISO): Geneva, Switzerland, 2011.
29. Zheng, B.; Jiang, G.; Wang, W.; Mei, X.; Wang, F. Surface ablation and threshold determination of AlCu4SiMg aluminum alloy in picosecond pulsed laser micromachining. *Opt. Laser Technol.* **2017**, *94*, 267–278. [CrossRef]
30. Lin, X.; Zhao, Y.; Liu, X.; Li, D.; Shuai, K.; Ma, H.; Shao, Y.; Sun, J.; Qiu, K.; Cui, Y.; et al. Damage characteristics of pulse compression grating irradiated by a nanosecond laser. *Opt. Mater. Express* **2022**, *12*, 643–652. [CrossRef]